



OPEN

Passive performance evaluation and validation of a viscous impeller pump for subpulmonary fontan circulatory support

Weiguang Yang^{1✉}, Timothy A. Conover², Richard S. Figliola², Guruprasad A. Giridharan³, Alison L. Marsden^{1,4} & Mark D. Rodefeld⁵

Patients with single ventricle defects undergoing the Fontan procedure eventually face Fontan failure. Long-term cavopulmonary assist devices using rotary pump technologies are currently being developed as a subpulmonary power source to prevent and treat Fontan failure. Low hydraulic resistance is a critical safety requirement in the event of pump failure (0 RPM) as a modest 2 mmHg cavopulmonary pressure drop can compromise patient hemodynamics. The goal of this study is therefore to assess the passive performance of a viscous impeller pump (VIP) we are developing for Fontan patients, and validate flow simulations against in-vitro data. Two different blade heights (1.09 mm vs 1.62 mm) and a blank housing model were tested using a mock circulatory loop (MCL) with cardiac output ranging from 3 to 11 L/min. Three-dimensional flow simulations were performed and compared against MCL data. In-silico and MCL results demonstrated a pressure drop of < 2 mmHg at a cardiac output of 7 L/min for both blade heights. There was good agreement between simulation and MCL results for pressure loss (mean difference – 0.23 mmHg 95% CI [0.24–0.71]). Compared to the blank housing model, low wall shear stress area and oscillatory shear index on the pump surface were low, and mean washout times were within 2 s. This study demonstrated the low resistance characteristic of current VIP designs in the failed condition that results in clinically acceptable minimal pressure loss without increased washout time as compared to a blank housing model under normal cardiac output in Fontan patients.

The Fontan procedure is the third and final stage of the typical palliative surgical sequence for children born with single ventricle heart defects. In the Fontan procedure, the inferior vena cava (IVC) is routed to the pulmonary artery (PA) via an extracardiac expanded polytetrafluoroethylene (ePTFE) graft or intra-atrial lateral tunnel baffle. Systemic venous return is completely diverted to the PA forming a total cavopulmonary connection (TCPC) after Fontan completion. Despite greatly reduced early death following the Fontan procedure, long term morbidity and mortality remain a concern. This is mainly due to inefficiencies inherent in a univentricular Fontan circulation, which lacks a functional subpulmonary ventricle and therefore results in non-pulsatile and non-energy-boosted flow to the lungs. Recent studies have shown that Fontan failure and late complications are responsible for 30 out of 40 deaths, with freedom from late Fontan complications of only 53% and 31% at 5 and 20 years, respectively¹. Overall 30-year survival after Fontan repair is only 43% for a single center cohort of 1052 patients².

Fontan physiology produces near-normal oxygen saturation at the expense of elevated systemic venous pressure, relative pulmonary arterial hypotension and reduced cardiac output compared to a normal biventricular physiology; these factors form the basis of the so-called “Fontan paradox”. Chronic and progressive elevation in systemic venous pressure, liver, intestinal, and lymphatic disorders, subnormal cardiac output, and elevated pulmonary capillary wedge pressure and systemic vascular resistance all contribute to the syndromic constellation of Fontan-associated disease³. Interestingly, however, in a large portion of patients with failing Fontan

¹Department of Pediatrics (Cardiology), Stanford University, Stanford, CA, USA. ²Departments of Mechanical Engineering, Clemson University, Clemson, SC, USA. ³Department of Bioengineering, University of Louisville, Louisville, KY, USA. ⁴Department of Bioengineering, Stanford University, Stanford, CA, USA. ⁵Section of Cardiothoracic Surgery, Department of Surgery, Indiana University School of Medicine, Indianapolis, IN, USA. ✉email: wgyang@stanford.edu

physiology, ventricular systolic function remains preserved⁴. This suggests that Fontan failure is not secondary to primary pump failure, but is rather secondary to chronic preload deprivation which has been postulated to lead to pathologic ventricular remodeling and diastolic dysfunction that contribute to progression of late Fontan failure^{3,5}. In other words, Fontan failure is not a failure of the single ventricle per se, but is rather a failure to fill the ventricle. Given this, we postulated that the “Fontan paradox” can be reversed by adding a mechanical cavopulmonary assist device that is capable of creating a subpulmonary pressure rise of 5–7 mmHg from the vena cavae to the PAs so that the systemic venous pressure could be reduced without reducing pulmonary flow and systemic ventricular preload to emulate a normal 2-ventricle circulation. For example, in Fontan patients, a desirable condition for a 7 mmHg increase in pressure head caused by the pump could lead to a 2–3 mmHg reduction on the caval side and a 4–5 mmHg increase on the PA side, assuming that the vena caval pressure is equal to the PA pressure prior to VIP support.^{6–8}

Although ventricular assist devices (VADs) have been used for failing Fontan patients as a bridge to heart transplant^{9–11}, existing mechanical circulatory assist devices are mainly designed for the high-pressure systemic circulation and are ill-suited for use in the Fontan circulation, which requires only a modest pressure rise. It is however critical to assure long-term patency of the Fontan circuit in the event of pump failure. Rodefeld et al.¹² proposed a viscous impeller pump (VIP) design inspired by the von Karman viscous pump which allows for 4 direction flow augmentation using a single pump. Several groups have followed with proof of concept for similar Fontan pumps, based on shrouded impeller designs^{13,14}. In addition, axial flow pump designs have been pursued for supporting the Fontan circulation as well^{6,15–18}.

Our team is further refining the VIP design toward the goal of clinical translation. The pump utilizes an outrunner motor configuration in which an outer biconical rotating component consists of permanent magnets and 4 hydraulic blades on each side, with stationary motor windings located centrally. The pump is secured by six struts welded to a titanium housing and suspended in the midst of the cavopulmonary junction so that blood flow from the SVC and IVC travels through the patent space between the housing wall and outer biconical rotors and get augmented continuously. A thin film secondary flow path allows a portion of flow to provide bearing lubrication and heat dissipation. The pump is connected to the native vessels via ePTFE grafts. Preliminary data show that a prototype pump can achieve a pressure head up to 14 mmHg at 5600 revolutions per minute (RPM) with no measurable gradient to passive Fontan flow at 0 RPM⁸.

The requirement for long-term patency of the Fontan circuit in the event of pump failure poses a design challenge as one must balance the tradeoff between competing objectives for active and passive flow. On one hand, the device should provide the desired pressure head rise with best possible efficiency; on the other hand, it should provide minimal internal resistance for a broad range of performance across various metabolic states, have low propensity for suction and cavitation, and most importantly not obstruct the Fontan circuit in the event of rotational failure. Note that a modest 2 mmHg pressure drop in Fontan passive flow can compromise pulmonary afterload and cardiac output requiring intervention¹⁹. In prior work, we have applied the surrogate management framework (SMF) to optimize the palliative surgeries for single ventricle defects^{20–23}. However, before design optimization can be carried out for VIPs, it is necessary to validate our baseline simulations against in-vitro experimental data under passive flow conditions. Thus, the goal of this study is to compare the pressure gradient across the pump at 0 RPM predicted by computational fluid dynamics (CFD) to experimental measurements in a mock circulatory loop (MCL) for a wide range of flow conditions and to characterize the passive hemodynamic performance of current VIP designs. The active hemodynamic performance under rotating conditions is presented in a separate study²⁴.

Methods

Mock circulatory loop. The MCL is an in-vitro test platform consisting of hydraulic and mechanical components to simulate blood circulation under healthy and pathological conditions. Previously MCLs have been extensively used to characterize hemodynamics in congenital heart diseases and VADs^{25–30}. The VIP was installed inside a transparent pump housing with 2 inlets and 2 outlets connected to the pipes that represent the venae cavae and the PAs, respectively (Fig. 1a,b). To test the influence of geometry, two impeller designs and a blank housing model were compared (Fig. 1c–e). The baseline design contained blades with a height of 1.09 mm while in the modified design, the blade height was increased to 1.62 mm and edge fillets were used to smooth sharp edges. The impeller and rotor hub surface were 3D printed by Pro Jet 700HD (3D Systems, Rock Hill, SC, USA) using a translucent polycarbonate like material (Accura ClearVue) with a smooth and glossy finish and mounted to the rotor. The printer is capable of reproducing features down to 0.05 mm. As a control, the blank housing model had the identical geometry except with no pump and struts inside.

In the upstream and downstream portions of the test section, five blocks of physical lumped parameter models (LPMs) were used to model the circulation in the lower body, upper body, splanchnic organs and two lungs (Fig. 1b). The resistance elements in the MCL were implemented by adjustable ball valves and laminar flow elements in which bundles of small elastic tubes with diameters ranging from 0.75 to 3 mm were packed together. The systemic compliance elements in MCL were implemented by “windkessels” which are cylinders ($D = 102$ mm) containing specific volumes of trapped air²⁸. The two pulmonary compliance elements employ the hydrostatic principle, each having a specific area of free surface in a vertical prism to create pressure proportionate to stored volume.

Two computer-controlled gear pumps were used to independently drive upper and lower body flow, and therefore SVC and IVC flow, with a split ratio of 60/40 (IVC/SVC) in this study. The MCL is capable of generating programmed time-varying flow. In this study, however, steady flow was generated for 5 cardiac output (CO) values of 3.0, 5.0, 7.0, 9.0 and 11.0 L/min. Atrial pressure of 7.5 mmHg was maintained by a constant head tank. A glycerol/water mixture with a weight ratio of 40/60 (mass ratio) is used as a blood analog fluid with a

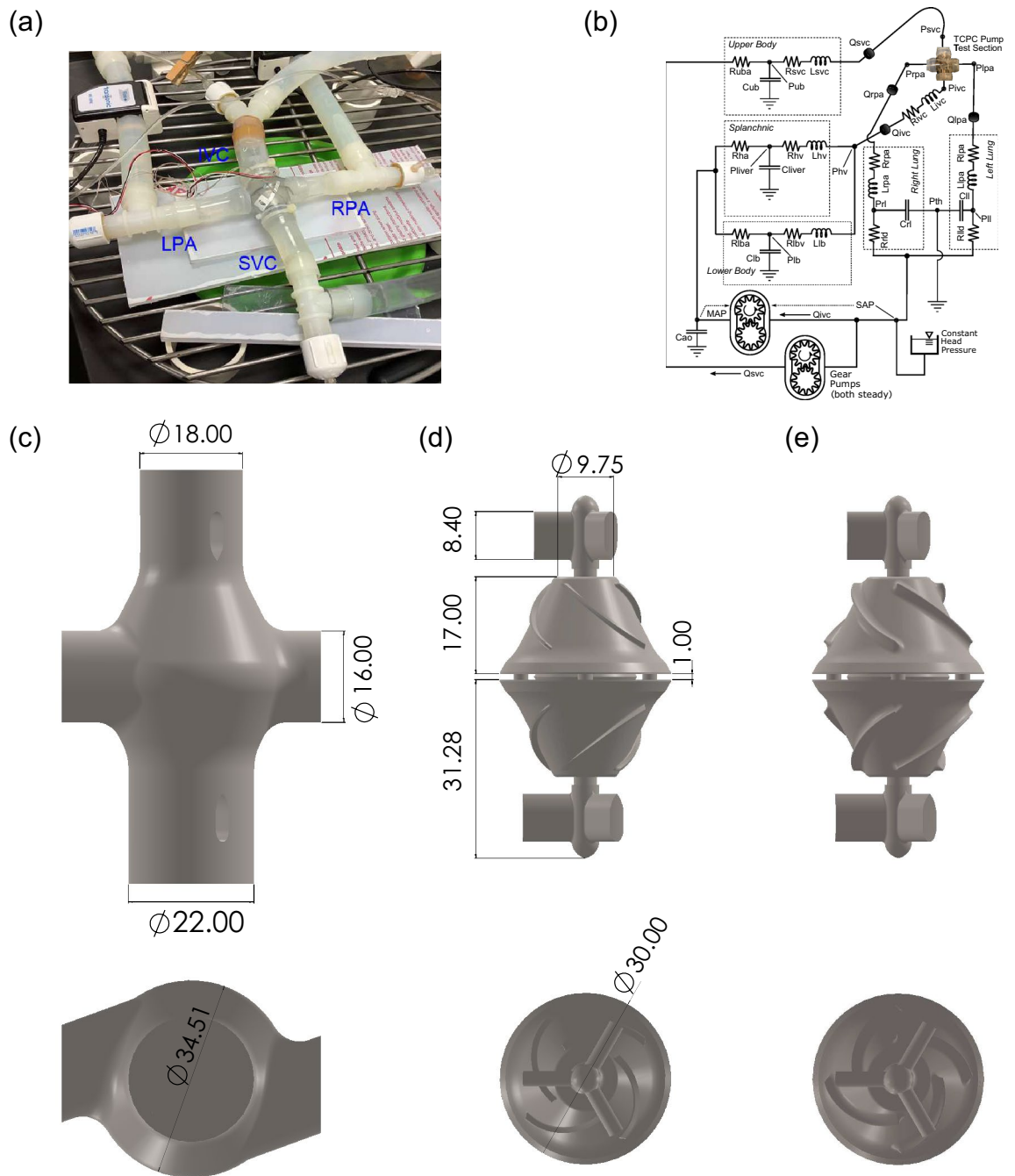


Figure 1. MCL layout and VIP prototype design. **(a)** MCL Test section. Several Y and T shaped tube fittings are used at the inlets and outlets of the test section for catheter access. The internal diameter for inflow and outflow tubing is 1.91 cm. **(b)** A diagram of the mock circulatory system. Physical lumped parameter models are coupled to the pump forming a closed loop circulation where R, C and L represent resistors, capacitors and inductors, respectively, and Q and P represent volumetric flow rates and pressures, respectively. MAP mean arterial pressure, SAP single atrial pressure, *th* throacic, *ll* left lung, *rl* right lung, *lld* left lung distal, *rlld* right lung distal, *ha* hepatic artery, *hv* hepatic vein and *ao* aorta. **(c)** The VIP housing, containing the impeller, replaces the cruciform TCPC. **(d)** The baseline VIP design employs 4 impellers with a height of 1.09 mm for each inlet. **(e)** The modified design increases the blade height to 1.62 mm with edge fillets. Dimensions are in mm.

density of 1.06 g/cm³ and a viscosity of 0.035 Poise. The changes in fluid temperature were within 1 °C. Based on a diameter of 1.91 cm for the inflow tubing and IVC flow, the Reynolds number was 674, 1015, 1433, 1839 and 2250 for CO = 3.0, 5.0, 7.0, 9.0 and 11.0 L/min, respectively. The pulmonary impedance networks caused the RPA and LPA outflow pressures to vary according to 6.0 + 0.74 × CO and 6.0 + 0.77 × CO, respectively. The

inclusion of time-based elements under nominal steady flow conditions can provide a mechanism to observe any flow instability or surging associated with the pump and its interactions with the circulation. However, no such activity was observed during the experiments. Four liquid-filled pressure catheters were placed at 4 cm from the pump housing center. Volumetric flow rates were measured by ultrasonic flow sensors installed at the upstream and downstream of each inlet and outlet, respectively. An in-house Labview program was used for data acquisition. Pressure and flow signals were filtered by 4th-order and 1st-order filters, respectively, before sampling. Pressure and flow drifts were maintained at or below 0.1 mmHg and 0.01 L/min, respectively, with 95% confidence during the initial and final all-stop measurements.

Passive flow simulations. The test section and its adjacent tubing were created using SolidWorks 2019 (Dassault Systèmes SolidWorks Corporation, Waltham, MA, USA). The solid file was discretized into linear tetrahedral elements using the MeshSim software library (Simmetrix Inc., Clifton, NY, USA). The general isotropic mesh size and the tubing surface mesh size were set to 0.2 and 0.09 cm respectively. To represent the complex geometry of the pump, the surface mesh size for impellers and struts was reduced to 0.03 cm and 0.06, respectively. To improve the resolution near the wall, we used a boundary layer mesh in which the mesh size at the n -th innermost layer is reduced to $\frac{1}{2^n}h$, where h is the general isotropic mesh size. To reduce computational cost, n was set to 3 and 1 for the central test section and peripheral tubing, respectively. The resulting mesh consists of 7.9 and 3 million tetrahedral elements for a model with a VIP and a blank housing model respectively. The mean tetrahedron aspect ratio, minimum dihedral angle and shape of the baseline VIP model are 2.14, 39.55 and 0.69, respectively. A mesh sensitivity study was performed by comparing the pressure loss at the highest cardiac output for the baseline VIP design on coarsened and refined meshes. The differences in pressure loss were within 3%. Additional details are presented in the supplementary materials.

The stabilized finite element Navier-Stokes solver svSolver available open source via the SimVascular project (<https://simvascular.github.io/>)^{31–33} was employed to simulate the flow testing. The source code for the flow solver is available on Github (<https://github.com/SimVascular/svSolver>). The weak form for incompressible Newtonian flow with no-slip rigid walls is as follows, Find $\{v, p\} \in S$ for any $\{w, q\} \in W$ such that

$$B_G(w, q; v, p) = \int_{\Omega} w \cdot (\rho v_{,t} + \rho v \cdot \nabla v - f) d\Omega + \int_{\Omega} \nabla w : (-p\mathbf{I} + \boldsymbol{\tau}) d\Omega - \int_{\Gamma_h} \{w \cdot \mathbf{h}\} d\Gamma + \int_{\Omega} q \nabla \cdot v d\Omega = 0, \quad (1)$$

where v and p are velocity and pressure in trial solutions space S , respectively, w and q are weighting functions for the momentum and continuity equations in weighting space W respectively, f and $\boldsymbol{\tau}$ are body force and viscous stress tensor respectively, Ω represents the fluid domain, and Γ_h represents Neumann boundaries with traction forces \mathbf{h} prescribed on vessel outlet faces. Note that Eq. (1) was augmented to include residual based stabilization terms^{34,35} in the solver to overcome the instability due to advection-dominated flow and the equal order interpolation of velocity and pressure. A second-order generalized- α method was employed for time integration and a Newton-Raphson method was employed to solve the nonlinear equation at the correction step³⁶. In addition, outlet back flow stabilization³⁷ and resistance based preconditioning^{38,39} techniques were employed in the solver.

We imposed the flow rates measured in the MCL testing by prescribing parabolic velocity profiles at the inlets. At the outlets, we used a resistance boundary condition⁴⁰ in which the traction \mathbf{h} in Eq. (1) is related to downstream resistance R and outflow Q by $\mathbf{h} = -RQ\mathbf{n} = -R \int_{\Gamma} \mathbf{u} \cdot \mathbf{n} d\Gamma \mathbf{n}$. The resistance values for the RPA and LPA outlets were chosen to be 204.51 and 222.49 dyn \cdot s/cm³ to achieve the measured flow split (R52/L48) and PA pressures for the blank housing model at CO = 11 L/min and kept unchanged for other cases.

Steady flow simulations were performed for 5 s with a time step of 0.001 s. State files were saved every 0.02 s. A python script using the paraview.simple module was created to extract and average the pressures data on cut planes at 4 cm away from the origin from $t = 2$ s to $t = 5$ s for calculation. The risk of thrombosis is evaluated using common shear-stress-based endpoints. Low wall shear stress (WSS) and oscillatory shear index (OSI) are associated with flow recirculation that increases the risk of thrombosis. The time-averaged wall shear stress (TAWSS) and OSI are defined as follows,

$$\boldsymbol{\tau} = \boldsymbol{\sigma} \cdot \mathbf{n} - (\boldsymbol{\sigma} \cdot \mathbf{n} \cdot \mathbf{n})\mathbf{n},$$

$$TAWSS = \left| \frac{\int_0^T \boldsymbol{\tau} dt}{T} \right|,$$

$$OSI = \frac{1}{2} \left(1 - \frac{\left| \int_0^T \boldsymbol{\tau} dt \right|}{\int_0^T |\boldsymbol{\tau}| dt} \right), \quad (2)$$

where \mathbf{n} is the unit normal vector and $\boldsymbol{\sigma}$ is the stress tensor. Regions with TAWSS < 5 dyn/cm² are empirically defined as low WSS regions based on previous studies^{41–43}.

To characterize the regions of flow stasis, we placed a 3.5 \times 3.5 \times 3.5 cm cube of virtual dye with uniform concentration in the center of the pump and quantified the required time for the dye to be washed out. Similarly, a stabilized finite element solver was employed to solve the following weak form of the advection–diffusion equation⁴⁴.

Find $\phi \in S$ for any $q \in W$ such that

$$\int_{\Omega} q \cdot (\phi_{,t} + \rho \mathbf{v} \cdot \nabla \phi) d\Omega + \int_{\Omega} \nabla q \cdot (\kappa + \kappa_{DC}) \nabla \phi d\Omega + \Sigma_e \int_{\Omega_e} \nabla q \cdot \mathbf{v} \tau_m \mathcal{L}(\phi, \mathbf{v}) d\Omega = 0,$$

$$\tau_m(\mathbf{x}, t) = \frac{1}{\sqrt{4/dt^2 + \mathbf{v}^T \xi \mathbf{v} + 3(\kappa + \kappa_{DC})^2 \xi : \xi}} \quad (3)$$

$$\kappa_{DC} = \frac{|\mathcal{L}|}{2\sqrt{\nabla^T \phi \xi \nabla \phi}},$$

where ϕ is a scalar field representing the dye concentration, \mathbf{v} is the velocity field given by the solution of Eq. (1), κ and κ_{DC} are the diffusion coefficient and the discontinuity capturing diffusion coefficient, τ_m is the stabilization parameter and \mathcal{L} is the advection-diffusion operator $\mathcal{L} := \frac{\partial \phi}{\partial t} + \mathbf{v} \cdot \nabla \phi - \nabla \cdot \kappa \nabla \phi$.

The initial scalar field $\phi(\mathbf{x})$ was set to be 1 in the region of interest and 0 elsewhere. The boundary value at inlets were set to be 0. The washout time $T(\mathbf{x})$ is defined as the minimum time needed for ϕ to decrease to 1% of its maximum value so that:

$$T(\mathbf{x}) = \int_{t_{max}}^{t_{1\%}} dt, \quad (4)$$

where t_{max} is the time when ϕ starts to decay from the maximum value and $t_{1\%}$ is the time when ϕ reaches 1% of its maximum value at \mathbf{x} .

Results

Figure 2a–c show the differences in pressure loss between CFD and MCL at 3, 5, 7, 9 and 11 L/min. The largest difference from the experimental data (– 0.8 mmHg) was found in the 1.62 mm model at the highest flow rate of 11 L/min. Experimental data shows that the difference in pressure loss due to the changes in blade height (1.09 mm vs 1.62mm) was up to 1.1 mmHg at 11 L/min while simulations predicted a difference of 0.5 mmHg under the same condition. Compared to the blank housing model, the increased pressure loss due to the presence of a failed VIP is at most 0.7 mmHg at CO = 7 L/min. Figure 2d further compares the in-vitro pressure loss at 0 RPM between the VIPs and two shrouded pumps proposed by Graneger et al.^{14,45} and Cysyk et al.¹³. Compared to the VIP used in the present study, the pressure loss across a failed shrouded pump rises markedly with increasing flow.

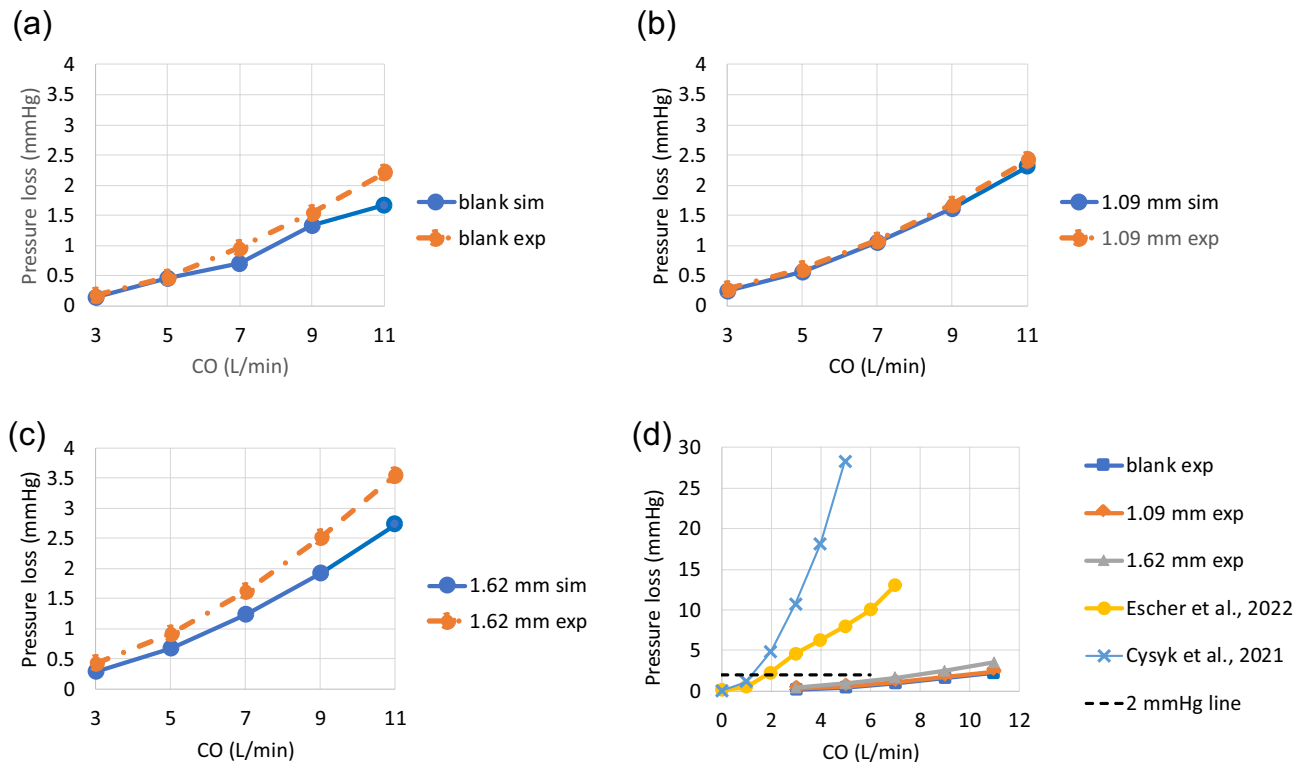


Figure 2. Pressure drops across (a) a blank housing and a static pump with (b) 1.09 mm blades and (c) 1.62 mm blades under 5 cardiac output values measured by simulations and MCS. In (d), in-vitro pressure loss data for 0 RPM are compared between the present study and previous studies by Escher et al.⁴⁵ and Cysyk et al.¹³ in which two shrouded Fontan pumps were studied. The dashed line at 2 mmHg represents the median pressure gradient for patients undergoing catheter-intervention due to Fontan pathway obstruction^{46,47}.

Differences between simulation and MCL data increased with increasing cardiac output (Fig. 3). Overall, there was good agreement and correlation between simulation and MCL results, though simulations tended to slightly under-predict the pressure drop compared to MCL.

Power loss caused by the pump and housing was compared to the values reported in previous Fontan simulation studies^{48–52}. The static pump resulted in a similar or smaller power loss compared to conventional and Y-shaped Fontan models (Supplementary Fig. S3).

Representative velocity fields in three models are visualized in Fig. 4. A recirculation zone is visible in the blank housing. The presence of a static VIP eliminates that recirculation zone and increases flow velocity though local flow separation remains and can be seen near the blades and the equator where the upper and lower rotors are connected. The use of edge fillets in the 1.62 mm design reduces the flow separation zone behind the blades compared to the 1.09 mm design without fillets. There are outward and inward flow motions near the secondary flow entrance underneath the struts.

Figure 5 shows the TAWSS distribution for the pump surface. Mean TAWSS values and the areas of low TAWSS ($< 5 \text{ dyn/cm}^2$) for different parts of the pump are shown in Fig. 6. The blank housing model resulted in a

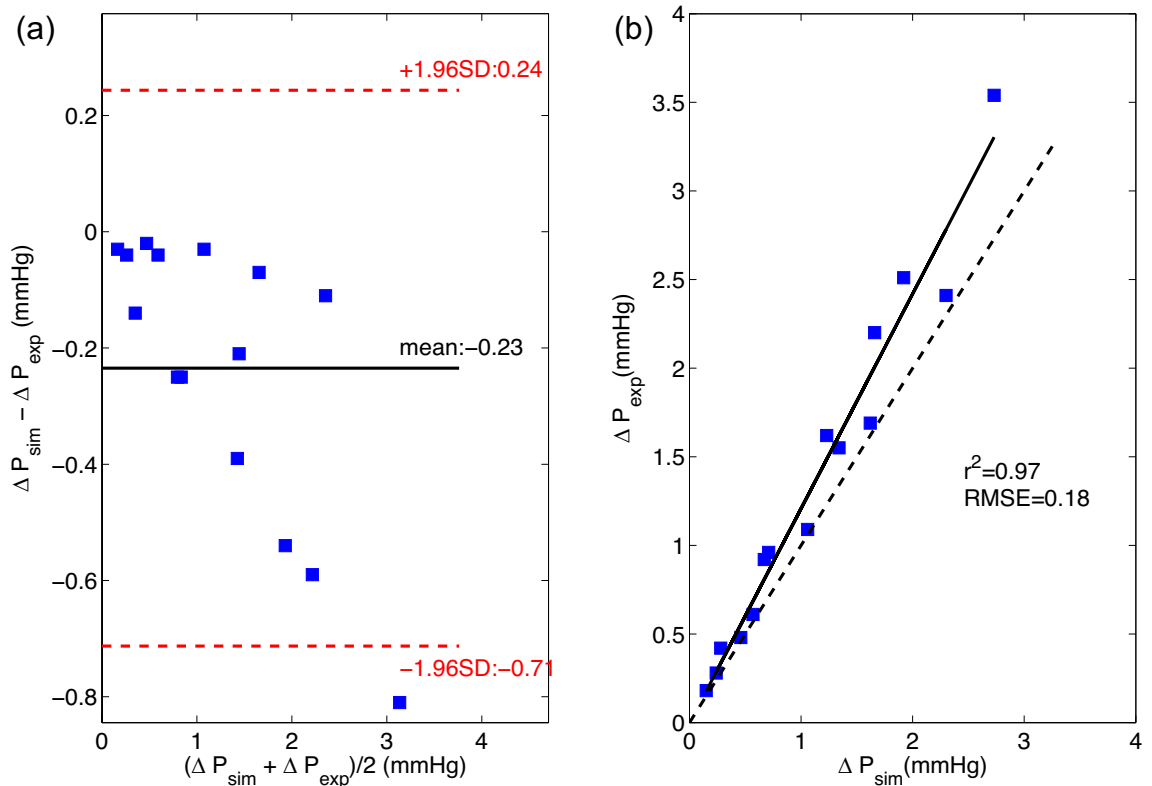


Figure 3. Bland–Altman (a) and correlation (b) plots for simulation and MCS derived pressure drop data.

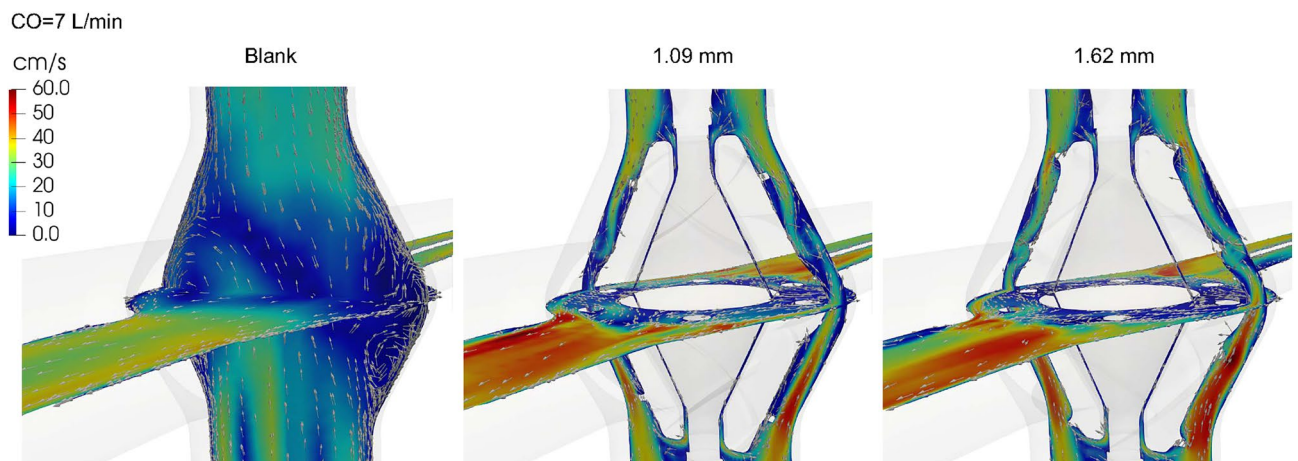


Figure 4. Mean velocity magnitude and vectors projected onto two central cut planes at 7 L/min.

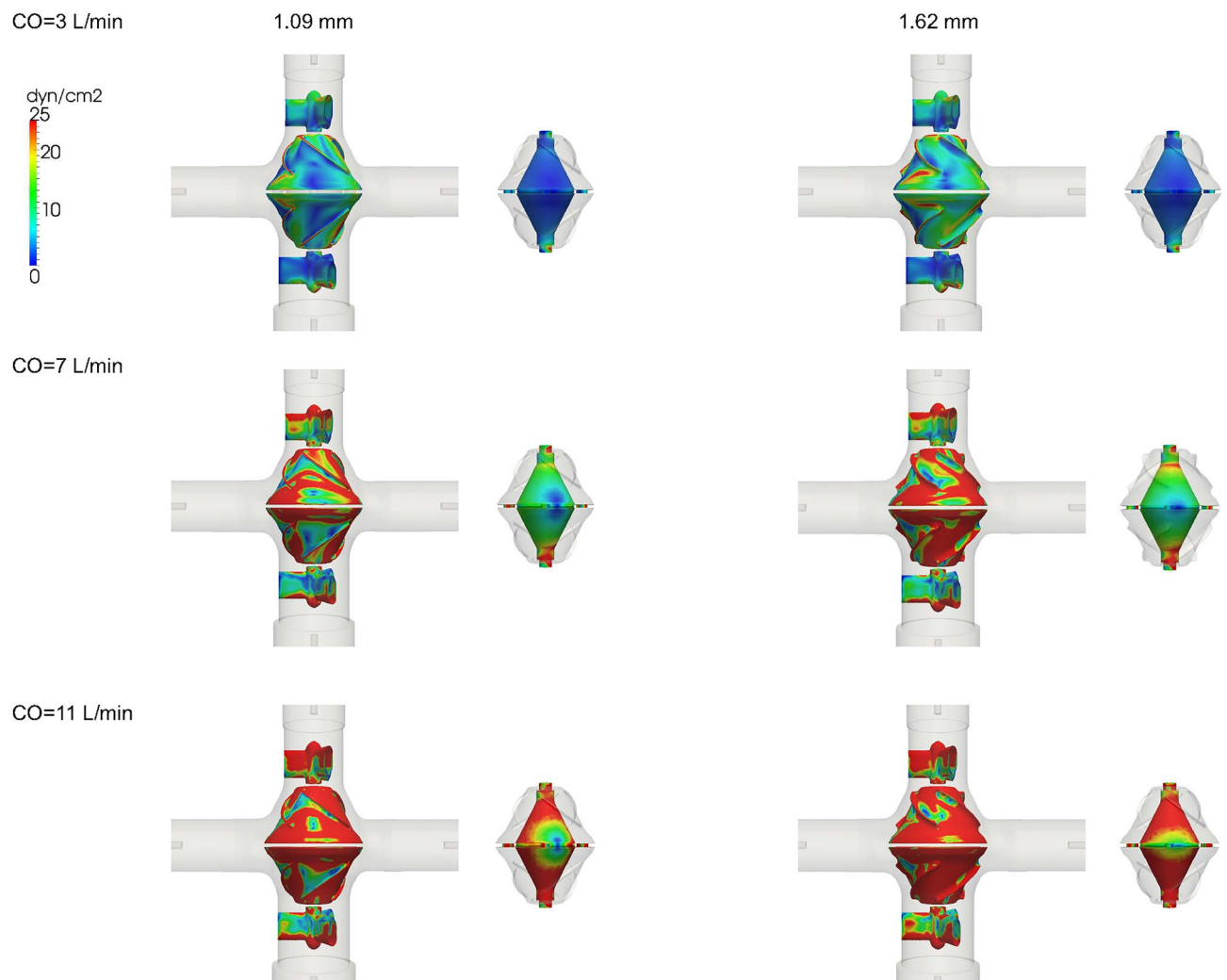


Figure 5. Time averaged wall shear stress (TAWSS) distribution on the rotor, strut and secondary flow surfaces for a 1.09 mm blade design and a filleted 1.62 mm blade design.

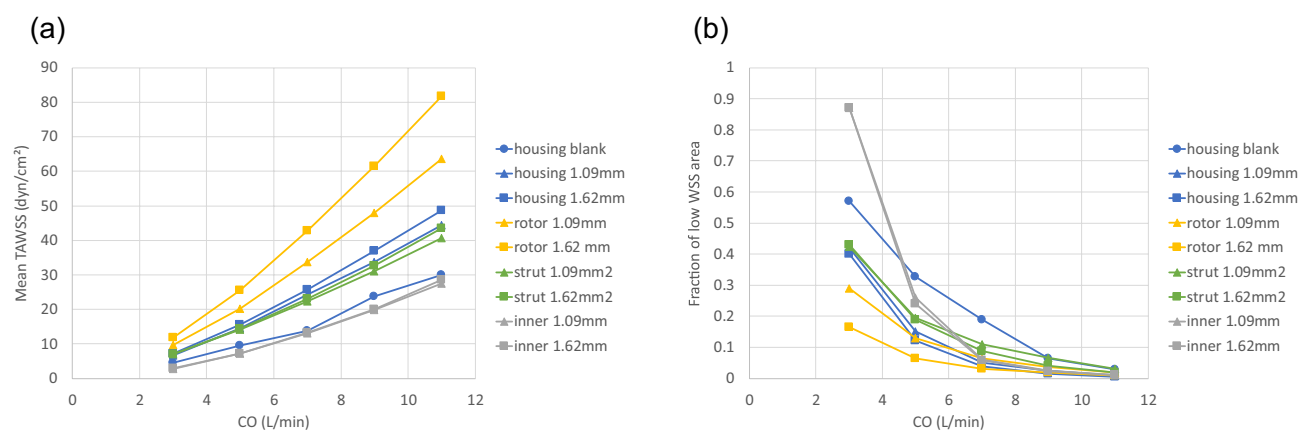


Figure 6. (a) Mean wall shear stress (WSS) and (b) area fraction of low WSS ≤ 5 dyn/cm² for the housing, rotor, strut and inner secondary flow surfaces.

lower WSS level and an increased region of low WSS on the housing surface compared to the models with a VIP inside (Supplementary Fig. S4). Compared to a conventional extracardiac Fontan graft ($D = 20$ mm)⁴⁸, there is a larger chamber at the junction in the blank housing model ($D_{\text{max}} = 34$ mm) creating more flow recirculation. Due to a reduced cross-sectional area for flow passage, mean TAWSS for both VIPs was greater than those of the blank housing model and increased with increasing blade height. Since flow in the secondary flow path was less than 1% of the total inflow at 0 RPM, a lower WSS level is expected there.

OSI on the rotor and strut surfaces was nearly zero for $\text{CO} \leq 5$ L/min. The size of the region with non-zero OSI increased with increasing CO due to flow separation past the rotor blades and struts (Supplementary Fig. S5). In contrast, the flow in the secondary path was nearly unidirectional regardless of cardiac output.

Figure 7 shows the dye concentration at $T = 0.04, 0.16, 0.64$ s for a $3.5 \times 3.5 \times 3.5$ cm cube of virtual dyes initially released at the center of the pump for $\text{CO} = 3$ L/min. Residual dyes are visible near the wall or in the secondary flow path only for the VIP models while the blank housing model still show a large amount of dyes in the center after 0.64 s (Fig. 7). With increased cardiac output, after 0.64 s, most dye is concentrated in the secondary flow path only for the VIP models while residual dye remains visible near the housing wall for the blank housing model (Supplementary Fig. S6). Figure 8 shows the mean washout time in the region of interest under all flow conditions. We found that it took more time to wash out the dyes in the blank housing model than in the VIP models where regions with high washout time were located in the secondary path and junctions only.

Discussion

Unlike the existing mechanical circulatory devices placed in parallel to the native circulation, the VIP is permanently implanted in-series in the lowest pressure venous segment of the human circulation. A minimal risk of flow obstruction in the event of mechanical failure is a critical safety requirement as the in-series placement creates complete circulatory dependency on flow passing through the device. Novel to blood pump design, a pump intended for Fontan circulatory support must thus be equally optimized to maximize required Fontan circulatory support while avoiding obstruction potential in its functional (rotating) state as well as its failed (non-rotating) state. Balancing the requirement for optimal pump function (hydraulic efficiency, head rise, low power requirement) with the need for minimal risk in a failed state (passive flow optimization, thrombogenicity risk mitigation) are competing objectives that are diametrically opposed, and present a unique challenge. Patients with Fontan circulation survive for decades after Fontan procedure. Current rotary blood pump technologies, while approved for destination therapy, are limited to 5–10 years of use. Thus, the challenge of having a failure tolerant, low pump resistance design that can provide adequate support when functional is critical to safely translate cavopulmonary assist to clinical practice.

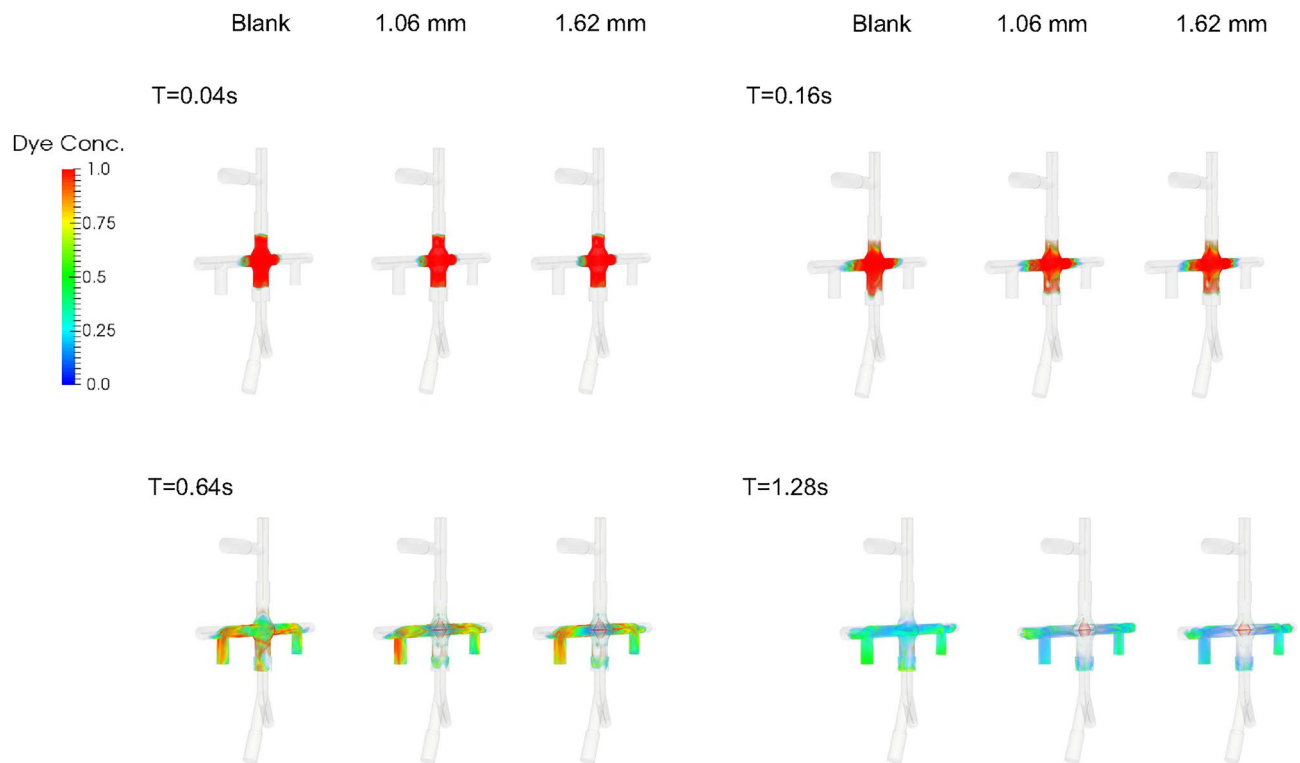


Figure 7. Dye concentration at $T = 0.04, 0.16, 0.64$ s for a blank housing, 1.09 mm blades and 1.62 mm blades at $\text{CO} = 3$ L/min. Virtual dyes with $\phi = 1$ were placed in the center of the pump at $T = 0$ and advected with flow.

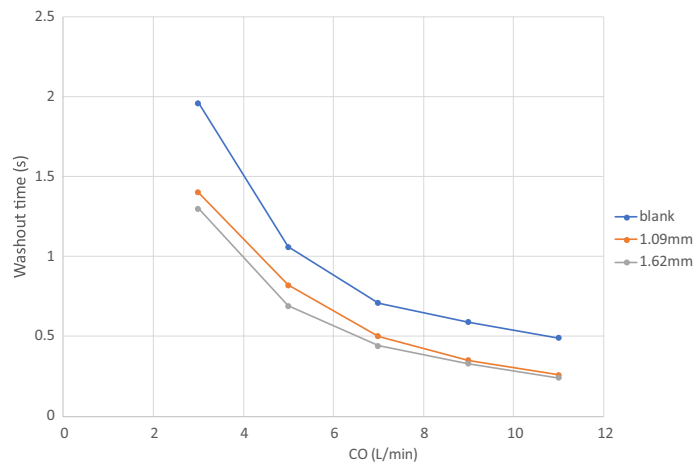


Figure 8. Mean washout time for dyes initially released in the pump under different flow conditions.

In this study, we validated the simulation predicted pressure loss for two VIP prototypes and a blank housing model under passive flow conditions (i.e. a non-rotating or “failed” pump at 0 RPM) against MCL testing data. Overall, there was excellent agreement for cardiac output values of 3, 5 and 7 L/min. The differences between simulations and MCL increased up to 0.8 mmHg for high cardiac outputs of 9 and 11 L/min due to increased flow disturbances. Despite steady inflow conditions, the flow field became unsteady with increasing cardiac output as flow separation and vortex shedding were created by the interactions between flow and internal structures including the pump blades, hub surface and struts. Factors that may have contributed to slightly higher discrepancies at higher cardiac output values include the catheter placement and geometric discrepancies between pump/tubing and discretized computational domains.

Although these pressure gradients may at first appear trivial, Fontan pathway narrowing and obstruction could be detrimental even in the absence of a measurable pressure gradient. No rigorous clinical cut-off value for treating Fontan obstruction has been established as the benefits and risks associated with the intervention need to be carefully weighed for each patient. It has been reported that the median pre-stenting pressure gradient was 2 mmHg for Fontan patients undergoing catheter-intervention for Fontan obstruction^{46,47}. Both MCL and numerical modeling confirmed a low resistance design. The mean pressure gradient at CO = 7 L/min for the stopped VIPs tested in this study is below 2 mmHg. The increased pressure loss at high cardiac output indicates adverse hemodynamics caused by a stopped VIP under exercise conditions. It is known that pressure loss across stenosis becomes nonlinear with increasing flow⁵³. Previous studies suggested that the nonlinear increase in power loss in the Fontan circuit under simulated exercise conditions may contribute to the exercise intolerance experienced by Fontan patients^{50,54,55}. Although there is an increasing trend, the power loss across a stopped VIP remains comparable to that of typical Fontan circuits during exercise (Supplementary Fig. S3). Our design intent is that at 0 RPM, the biconical design splits SVC and IVC flow without significantly increasing resistance. This failure mode is comparable to previous Fontan passive flow modifications such as the OptiFlo and Y-graft designs^{48,49,56–58}. In contrast, shrouded Fontan pumps proposed by others have reported a clinically untenable gradient of 13 mmHg for a flow rate of 7 L/min⁴⁵ and 18 mmHg for a flow rate of 4 L/min¹³. Fontan circuit gradients in this range would be clinically destabilizing and likely necessitate emergency surgical intervention for salvage. From a safety perspective, we believe that intrinsic low hydraulic resistance is essential for a long-term Fontan pump. In other words, a Fontan patient should never be dependent upon pump flow, or upon the pump remaining operational for survival. Considering the increased pressure loss during exercise, future studies should model the physiological responses to a previously failed VIP that has not been removed during mild exercise or a suddenly stopped VIP during high metabolic activity.

The design of a long term cavopulmonary assist device is subject to unique objective functions and constraints that may be in conflict with each other. Careful consideration must be made as placing emphasis on different aspects of pump performance may lead to diametrically opposed directions in the VIP design. With increased geometric complexity, we need to better understand the relationships between design parameters and quantities of interest. Design refinements could be better informed by the use of sensitivity analysis and shape optimization techniques in future studies^{20,23,59–62}.

In addition to low hydraulic resistance, risks of thrombosis also play a role in the long-term passive safety of VIPs. Despite a lack of accurate and reliable models for predicting thrombosis formation, three shear-stress-based endpoints were used to characterize flow stasis in the region of interest. Regions of low WSS in the VIP models were localized showing a smaller area fraction of low WSS compared to the blank housing model despite a larger blood contacting area in the pump. As compared to the 1.09 mm design, the increased mean WSS on the rotor surface (+ 27% at 7 L/min) and reduced low WSS area fraction (– 3% at 7 L/min) can be attributed to the use of edge fillets that improved flow separation despite a larger pressure drop in the 1.62 mm design. Overall mean TAWSS in the VIPs was in the physiologic range⁴³ and comparable to the mean TAWSS in the extra cardiac Fontan graft^{48,57,58} for CO = 3 and 5 L/min.

Similarly, dye washout time results agreed with the shear-based endpoints. Dye in the secondary flow path was trapped at 3 L/min taking more than 5 s to be washed out and making the secondary flow path prone to blood clots when the pump is stopped. However, the passive performance is unlikely to be affected by an obstructed secondary flow path given that < 1% of the venous return passes through the secondary flow path. Other flow stasis regions under low cardiac outputs include the junction between the housing and outlets, and the base of the conical rotor hub surface suggesting a local shape modification could be made to improve flow separation and recirculation. Overall, our simulation results did not identify concerning surrogate values for thrombotic potential.

Limitations

A major limitation of this study is the use of steady inflow conditions. Although unsteady vortex shedding and fluctuations developed with increasing cardiac output, the instantaneous flow field remains different from the natural condition with respiration-dependent pulsatile flow. For time-averaged quantities such as pressure drops and TAWSS, we expect to find similar trends among the three models tested in this study under pulsatile flow conditions. The increased pressure drop that would occur at the peak inspiratory flow would likely be similar to the results under higher steady flow conditions (9 and 11 L/min).

The passive performance for the VIP in a patient specific model was not evaluated in this study. Unlike the test section in which circular pipes were arranged on the same plane, there is a large variation in patient specific PAs. In future studies, patient specific models coupled with a closed loop lumped parameter network^{63–65} will be studied.

In addition, the flow split for the IVC/SVC was fixed at 60/40 and symmetric pulmonary flow distribution was only considered in this study. Previous studies showed that IVC flow fraction is correlated with age and body surface area^{66,67}, and unilateral pulmonary arteriovenous malformation can lead to skewed pulmonary flow distribution⁴¹. Thus, the impacts of uncertainties in inflow and outflows splits on pump active and passive performance should be studied to account for younger patients and patients with uncommon flow conditions in future studies.

A threshold value used for assessing low WSS has not been validated and the risks of thrombosis were compared relative to the blank housing model. It is well known that an oversized extracardiac Fontan graft is prone to thrombosis despite lower hydraulic resistance⁶⁸. The blank housing model with a bulging chamber at the Fontan junction creates extra space for mixing and recirculation resembling an oversized graft. However, these findings need to be validated compared to future in-vitro thrombosis studies, and furthermore, future hypothetical studies on the impact of clots virtually added to the pump surface will help to establish the performance envelop.

The fluid is assumed to be Newtonian. Although this is generally a valid approximation for flow in large vessels with large shear rates⁶⁹, non-Newtonian effects related to thrombogenesis may become important in flow recirculation where shear rates are low. Predictions for the locations where thrombi develop will be validated against future in-vitro and animal in-vivo studies.

In contrast to the naive vessels, the graft sections for the venae cavae and PAs in both MCL and flow simulations are not distensible. Future studies using realistic anatomic models could study the influence of variable material properties. Previously, Long et al.⁷⁰ showed that the wall motions could alter wall shear stress significantly despite little effect of FSI on pressure loss and hepatic flow distribution.

Conclusions

Both MCL and simulation results demonstrated that the latest VIP design created significantly lower pressure drops at 0 RPM under most flow conditions in Fontan patients, compared to other Fontan VADs. We observed good agreement between simulations and MCL results. Low WSS area and dye washout time in the pumps with both blade heights were smaller than those of a blank housing model. With an ≤ 0.5 mmHg increase in the pressure gradient at 0 RPM for CO = 3–7 L/min and greater hydraulic heads under working conditions, the 1.62 mm design with edge fillets is preferred to the 1.09 mm design. These findings will serve as a foundation for future design optimization to enhance the long-term passive safety features of cavopulmonary assist devices.

Data availability

The data generated during the current study are available from the corresponding author on reasonable request. The source code for the flow solver is available on Github (<https://github.com/SimVascular/svSolver>).

Received: 14 February 2023; Accepted: 11 July 2023

Published online: 04 August 2023

References

- Kotani, Y. *et al.* Fontan failure and death in contemporary fontan circulation: Analysis from the last two decades. *Ann. Thorac. Surg.* **105**, 1240–1247. <https://doi.org/10.1016/j.athoracsur.2017.10.047> (2018).
- Pundi, K. N. *et al.* 40-year follow-up after the fontan operation: Long-term outcomes of 1,052 patients. *J. Am. Coll. Cardiol.* **66**, 1700–1710. <https://doi.org/10.1016/j.jacc.2015.07.065> (2015).
- Hebson, C. L. *et al.* Hemodynamic phenotype of the failing fontan in an adult population. *Am. J. Cardiol.* **112**, 1943–1947. <https://doi.org/10.1016/j.amjcard.2013.08.023> (2013).
- Anderson, P. A. W. *et al.* Contemporary outcomes after the fontan procedure: A pediatric heart network multicenter study. *J. Am. Coll. Cardiol.* **52**, 85–98. <https://doi.org/10.1016/j.jacc.2008.01.074> (2008).
- Griffiths, E. R. *et al.* Evaluating failing Fontans for heart transplantation: Predictors of death. *Ann. Thorac. Surg.* **88**, 558–563. <https://doi.org/10.1016/j.athoracsur.2009.03.085> (2009) (**discussion 563–564**).
- Rodefeld, M. D. *et al.* Cavopulmonary assist: Circulatory support for the univentricular Fontan circulation. *Ann. Thorac. Surg.* **76**, 1911–1916. [https://doi.org/10.1016/s0003-4975\(03\)01014-2](https://doi.org/10.1016/s0003-4975(03)01014-2) (2003) (**discussion 1916**).

7. Leval, M. R. D. The Fontan circulation: A challenge to William Harvey?. *Nat. Clin. Pract. Cardiovasc. Med.* **2**, 202–208 (2005).
8. Rodefeld, M. D. *et al.* Cavopulmonary assist: Long-term reversal of the Fontan paradox. *J. Thorac. Cardiovasc. Surg.* **158**, 1627–1636. <https://doi.org/10.1016/j.jtcvs.2019.06.112> (2019).
9. VanderPluym, C. J., Rebecka, I. M., Ross, D. B. & Buchholz, H. The use of ventricular assist devices in pediatric patients with univentricular hearts. *J. Thorac. Cardiovasc. Surg.* **141**, 588–590. <https://doi.org/10.1016/j.jtcvs.2010.06.038> (2011).
10. Lorts, A., Villa, C., Riggs, K. W., Broderick, J. & Morales, D. L. S. First use of HeartMate 3 in a failing fontan circulation. *Ann. Thorac. Surg.* **106**, e233–e234. <https://doi.org/10.1016/j.athoracsur.2018.04.021> (2018).
11. Cedars, A. *et al.* Systemic ventricular assist device support in Fontan patients: A report by ACTION. *J. Heart Lung Transplant.* **40**, 368–376. <https://doi.org/10.1016/j.healun.2021.01.011> (2021).
12. Rodefeld, M. D. *et al.* Cavopulmonary assist for the univentricular Fontan circulation: von Kármán viscous impeller pump. *J. Thorac. Cardiovasc. Surg.* **140**, 529–536. <https://doi.org/10.1016/j.jtcvs.2010.04.037> (2010).
13. Cysyk, J. *et al.* Chronic in vivo test of a right heart replacement blood pump for failed fontan circulation. *ASAIO J. Am. Soc. Artif. Intern. Organs* **1992** **65**, 593–600. <https://doi.org/10.1097/MAT.0000000000000888> (2019).
14. Granegger, M. *et al.* A long-term mechanical cavopulmonary support device for patients with Fontan circulation. *Med. Eng. Phys.* **70**, 9–18. <https://doi.org/10.1016/j.medengphy.2019.06.017> (2019).
15. Riemer, R. K., Amir, G., Reichenbach, S. H. & Reinhartz, O. Mechanical support of total cavopulmonary connection with an axial flow pump. *J. Thorac. Cardiovasc. Surg.* **130**, 351–354. <https://doi.org/10.1016/j.jtcvs.2004.12.037> (2005).
16. Wei, X. *et al.* Mechanical circulatory support of a univentricular Fontan circulation with a continuous axial-flow pump in a piglet model. *ASAIO J. (Am. Soc. Artif. Intern. Organs)* **1992** **61**, 196–201. <https://doi.org/10.1097/MAT.0000000000000172> (2015).
17. Zhu, J. *et al.* Cavopulmonary support with a microaxial pump for the failing Fontan physiology. *ASAIO J. (Am. Soc. Artif. Intern. Organs)* **1992** **61**, 49–54. <https://doi.org/10.1097/MAT.0000000000000162> (2015).
18. Kafagy, D. H. *et al.* Design of axial blood pumps for patients with dysfunctional fontan physiology: Computational studies and performance testing. *Artif. Organs* **39**, 34–42. <https://doi.org/10.1111/aor.12443> (2015).
19. Stumper, O. & Penford, G. Catheter hemodynamic assessment of the univentricular circulation. *Ann. Pediatr. Cardiol.* **10**, 167–174. https://doi.org/10.4103/apc.APC_160_16 (2017).
20. Yang, W., Feinstein, J. A. & Marsden, A. L. Constrained optimization of an idealized Y-shaped baffle for the Fontan surgery at rest and exercise. *Comput. Method Appl. Mech. Eng.* **199**, 2135–2149 (2010).
21. Moghadam, M. E. *et al.* Optimization of shunt placement for the Norwood surgery using multi-domain modeling. *J. Biomech. Eng.* **134**, 051002. <https://doi.org/10.1115/1.4006814> (2012).
22. Yang, W., Feinstein, J. A., Shadden, S. C., Vignon-Clementel, I. E. & Marsden, A. L. Optimization of a Y-graft design for improved hepatic flow distribution in the fontan circulation. *J. Biomech. Eng.* **135**, 011002 (2013).
23. Verma, A. *et al.* Optimization of the assisted bidirectional Glenn procedure for first stage single ventricle repair. *World J. Pediatr. Congenit. Heart Surg.* **9**, 157–170. <https://doi.org/10.1177/2150135117745026> (2018).
24. Conover, T. *et al.* BIO6: Development and Testing of a Non-obstructive, Long-term. Cavopulmonary assist device. *ASAIO J.* **68**, 11–12. <https://doi.org/10.1097/01.mat.0000840760.63524.ea> (2022).
25. Figliola, R. S. *et al.* In vitro simulation and validation of the circulation with congenital heart defects. *Progr. Pediatr. Cardiol.* **30**, 71–80 (2010).
26. Kung, E. O. *et al.* In vitro validation of finite element analysis of blood flow in deformable models. *Ann. Biomed. Eng.* **39**, 1947–1960. <https://doi.org/10.1007/s10439-011-0284-7> (2011).
27. Giridharan, G. A. *et al.* Performance evaluation of a pediatric viscous impeller pump for Fontan cavopulmonary assist. *J. Thorac. Cardiovasc. Surg.* **145**, 249–257. <https://doi.org/10.1016/j.jtcvs.2012.01.082> (2013).
28. Vukicevic, M. *et al.* Control of respiration-driven retrograde flow in the subdiaphragmatic venous return of the Fontan circulation. *ASAIO J. (Am. Soc. Artif. Intern. Organs)* **1992** **60**, 391–399. <https://doi.org/10.1097/MAT.0000000000000093> (2014).
29. Zhou, J. *et al.* In vitro assessment of the assisted bidirectional Glenn procedure for stage one single ventricle repair. *Cardiovasc. Eng. Technol.* **6**, 256–267. <https://doi.org/10.1007/s13239-015-0232-z> (2015).
30. Giridharan, G. A. *et al.* Hemodynamic changes and retrograde flow in LVAD failure. *ASAIO J. (Am. Soc. Artif. Intern. Organs)* **1992** **61**, 282–291. <https://doi.org/10.1097/MAT.0000000000000200> (2015).
31. Schmidt, J. P. *et al.* The simbios national center: Systems biology in motion. *Proc. IEEE Spec. Issue Comput. Syst. Biol.* **96**, 1266–1280 (2008).
32. Updegrove, A. *et al.* SimVascular: An open source pipeline for cardiovascular simulation. *Ann. Biomed. Eng.* **45**, 525–541. <https://doi.org/10.1007/s10439-016-1762-8> (2017).
33. Lan, H. *et al.* A re-engineered software interface and workflow for the open-source SimVascular cardiovascular modeling package. *J. Biomech. Eng.* <https://doi.org/10.1115/1.4038751> (2018).
34. Taylor, C. A., Hughes, T. J. R. & Zarins, C. K. Finite element modeling of blood flow in arteries. *Comput. Method. Appl. Mech. Eng.* **158**, 155–196 (1998).
35. Whiting, C. H. & Jansen, K. E. A stabilized finite element method for the incompressible Navier–Stokes equations using a hierarchical basis. *Int. J. Numer. Methods Fluids* **35**, 93–116 (2001).
36. Jansen, K. E., Whiting, C. H. & Hulbert, G. M. A generalized- α method for integrating the filtered Navier–Stokes equations with a stabilized finite element method. *Comput. Method Appl. Mech. Eng.* **190**, 305–319 (2000).
37. Moghadam, M. E. *et al.* A comparison of outlet boundary treatments for prevention of backflow divergence with relevance to blood flow simulations. *Comput. Mech.* **48**, 277–291. <https://doi.org/10.1007/s00466-011-0599-0> (2011).
38. Esmaily-Moghadam, M., Bazilevs, Y. & Marsden, A. L. A new preconditioning technique for implicitly coupled multidomain simulations with applications to hemodynamics. *Comput. Mech.* **52**, 1141–1152. <https://doi.org/10.1007/s00466-013-0868-1> (2013).
39. Esmaily-Moghadam, M., Bazilevs, Y. & Marsden, A. L. A bi-partitioned iterative algorithm for solving linear systems arising from incompressible flow problems. *Comput. Methods Appl. Mech. Eng.* **286**, 40–62. <https://doi.org/10.1016/j.cma.2014.11.033> (2015).
40. Vignon-Clementel, I. E., Figueroa, C. A., Jansen, K. E. & Taylor, C. A. Outflow boundary conditions for three-dimensional finite element modeling of blood flow and pressure in arteries. *Comput. Method. Appl. Mech. Eng.* **195**, 3776–3796 (2006).
41. Yang, W., Chan, F. P., Reddy, V. M., Marsden, A. L. & Feinstein, J. A. Flow simulations and validation for the first cohort of patients undergoing the Y-graft Fontan procedure. *J. Thorac. Cardiovasc. Surg.* **149**, 247–255. <https://doi.org/10.1016/j.jtcvs.2014.08.069> (2015).
42. Casa, L. D. C., Deaton, D. H. & Ku, D. N. Role of high shear rate in thrombosis. *J. Vasc. Surg.* **61**, 1068–1080. <https://doi.org/10.1016/j.jvs.2014.12.050> (2015).
43. Hathcock, J. J. Flow effects on coagulation and thrombosis. *Arteriosclerosis Thromb. Vasc. Biol.* **26**, 1729–1737. <https://doi.org/10.1161/01.ATV.0000229658.76797.30> (2006).
44. Esmaily-Moghadam, M., Hsia, T.-Y. & Marsden, A. L. A non-discrete method for computation of residence time in fluid mechanics simulations. *Phys. Fluids* **25**, 110802. <https://doi.org/10.1063/1.4819142> (2013).
45. Escher, A. *et al.* A cavopulmonary assist device for long-term therapy of fontan patients. *Semin. Thorac. Cardiovasc. Surg.* **34**, 238–248. <https://doi.org/10.1053/j.semtcvs.2021.06.016> (2022).
46. Mets, J. M., Bergersen, L., Mayer, J. E. Jr., Marshall, A. C. & McElhinney, D. B. Outcomes of stent implantation for obstruction of intracardiac lateral tunnel Fontan pathways. *Circ. Cardiovasc. Interv.* **6**, 92–100. <https://doi.org/10.1161/CIRCINTERVENTIONS.112.000099> (2013).

47. Hagler, D. J. *et al.* Fate of the Fontan connection: Mechanisms of stenosis and management. *Congenit. Heart Dis.* **14**, 571–581. <https://doi.org/10.1111/chd.12757> (2019).
48. Yang, W. *et al.* Hepatic blood flow distribution and performance in traditional and Y-graft Fontan geometries: A case series computational fluid dynamics study. *J. Thorac. Cardiovasc. Surg.* **143**, 1086–1097 (2012).
49. Kanter, K. R. *et al.* Preliminary clinical experience with a bifurcated Y-graft Fontan procedure—A feasibility study. *J. Thorac. Cardiovasc. Surg.* **144**, 383–389 (2012).
50. Whitehead, K. K. *et al.* Nonlinear power loss during exercise in single-ventricle patients after the Fontan: insights from computational fluid dynamics. *Circulation* **116**, I-165–I-171 (2007).
51. Marsden, A. L., Vignon-Clementel, I. E., Chan, F., Feinstein, J. A. & Taylor, C. A. Effects of exercise and respiration on hemodynamic efficiency in CFD simulations of the total cavopulmonary connection. *Ann. Biomed. Eng.* **35**, 250–263 (2007).
52. Bove, E. L., de Leval, M. R., Migliavacca, F., Guadagni, G. & Dubini, G. Computational fluid dynamics in the evaluation of hemodynamic performance of cavopulmonary connections after the Norwood procedure for hypoplastic left heart syndrome. *J. Thorac. Cardiovasc. Surg.* **126**, 1040–1047 (2003).
53. Young, D. F., Cholvin, N. R. & Roth, A. C. Pressure drop across artificially induced stenoses in the femoral arteries of dogs. *Circ. Res.* **36**, 735–743. <https://doi.org/10.1161/01.res.36.6.735> (1975).
54. Sundareswaran, K. S. *et al.* The total cavopulmonary connection resistance: A significant impact on single ventricle hemodynamics at rest and exercise. *Am. J. Physiol. Heart Circ. Physiol.* **295**, H2427–2435. <https://doi.org/10.1152/ajpheart.00628.2008> (2008).
55. Tang, E. *et al.* Effect of Fontan geometry on exercise haemodynamics and its potential implications. *Heart (Br. Cardiac Soc.)* **103**, 1806–1812. <https://doi.org/10.1136/heartjnl-2016-310855> (2017).
56. Soerensen, D. D. *et al.* Introduction of a new optimized total cavopulmonary connection. *Ann. Thorac. Surg.* **83**, 2182–90 (2007).
57. Marsden, A. L. *et al.* Evaluation of a novel Y-shaped extracardiac Fontan baffle using computational fluid dynamics. *J. Thorac. Cardio. Surg.* **137**, 394–403 (2009).
58. Yang, W., Chan, F. P., Reddy, V. M., Marsden, A. L. & Feinstein, J. A. Flow simulations and validation for the first cohort of patients undergoing the y-graft fontan procedure. *J. Thorac. Cardiovasc. Surg.* **149**, 247–255 (2015).
59. Sankaran, S., Audet, C. & Marsden, A. L. A method for stochastic constrained optimization using derivative-free surrogate pattern search and collocation. *J. Comput. Phys.* **229**, 4664–4682 (2010).
60. Gundert, T. J., Marsden, A. L., Yang, W. & LaDisa, J. F. Optimization of cardiovascular stent design using computational fluid dynamics. *J. Biomech. Eng.* **134**, <https://doi.org/10.1115/1.4005542> (2012).
61. Gundert, T., Marsden, A., Yang, W., Marks, D. & LaDisa, J. Identification of hemodynamically optimal coronary stent designs based on vessel caliber. *IEEE Trans. Biomed. Eng.* **59**, 1992–2002. <https://doi.org/10.1109/TBME.2012.2196275> (2012).
62. Audet, C., Dennis, J. E. & Le Digabel, S. Trade-off studies in blackbox optimization. *Optim. Methods Softw.* **27**, 613–624. <https://doi.org/10.1080/10556788.2011.571687> (2012).
63. Baretta, A. *et al.* Virtual surgeries in patients with congenital heart disease: A multiscale modelling test case. *Philos. Trans. R. Soc.* **369**, 4316–4330 (2011).
64. Kung, E. *et al.* A simulation protocol for exercise physiology in Fontan patients using a closed loop lumped-parameter model. *J. Biomech. Eng.* <https://doi.org/10.1115/1.4027271> (2014).
65. Conover, T. *et al.* An interactive simulation tool for patient-specific clinical decision support in single-ventricle physiology. *J. Thorac. Cardiovasc. Surg.* **155**, 712–721. <https://doi.org/10.1016/j.jtcvs.2017.09.046> (2018).
66. Salim, M. A., DiSessa, T. G., Arheart, K. L. & Alpert, B. S. Contribution of superior vena caval flow to total cardiac output in children: A Doppler echocardiographic study. *Circulation* **92**, 1860–1865 (1995).
67. Whitehead, K. K. *et al.* Blood flow distribution in a large series of patients having the Fontan operation: A cardiac magnetic resonance velocity mapping study. *J. Thorac. Cardiovasc. Surg.* **138**, 96–102. <https://doi.org/10.1016/j.jtcvs.2008.11.062> (2009).
68. Alexi-Meskishvili, V. *et al.* Optimal conduit size for extracardiac Fontan operation. *Eur. J. of Cardio-Thorac. Surg.* **18**, 690–695 (2000).
69. Pedley, T. J. *The Fluid Mechanics of Large Blood Vessels*. Cambridge Monographs on Mechanics (Cambridge University Press, 1980).
70. Long, C. C., Hsu, M.-C., Bazilevs, Y., Feinstein, J. A. & Marsden, A. L. Fluid structure interaction simulations of the fontan procedure using variable wall properties. *Int. J. Numer. Method. Biomed. Eng.* **28**, 513–527 (2012).
71. Towns, J. *et al.* XSEDE: Accelerating scientific discovery. *Comput. Sci. Eng.* **16**, 62–74. <https://doi.org/10.1109/MCSE.2014.80> (2014).

Acknowledgements

The authors would like to thank Artem Ivashchenko, Michael Neary and Dr. Edward Bennett for sharing their CAD files and expertise. This study was supported by an NIH R01 Grant (5R01HL150346-02). Simulations were performed on the Expanse cluster at the San Diego Supercomputer Center through allocation TG-CTS130034 provided by the Extreme Science and Engineering Discovery Environment (XSEDE), which is supported by National Science Foundation grant number ACI-1548562⁷¹. The authors would like to thank Simmetrix Inc. for providing academic licenses for the MeshSim software library.

Author contributions

W.Y. conducted simulations and prepared the manuscript. T.C., R.F. and G.G. performed the MCL study. A.M., R.F. and M.R. conceptualized the study and supervised all aspects of the work. All authors analyzed and interpreted the results, and edited the manuscript.

Competing interests

Dr. Rodefeld discloses patent US 9,827,357 for cavopulmonary viscous impeller assist device and method. Dr. Giridharan provides consultations for NuPulseCV. His consulting work is unrelated to Fontan support. The remaining authors have no conflicts of interest to declare.

Additional information

Supplementary Information The online version contains supplementary material available at <https://doi.org/10.1038/s41598-023-38559-y>.

Correspondence and requests for materials should be addressed to W.Y.

Reprints and permissions information is available at www.nature.com/reprints.

Publisher's note Springer Nature remains neutral with regard to jurisdictional claims in published maps and institutional affiliations.



Open Access This article is licensed under a Creative Commons Attribution 4.0 International License, which permits use, sharing, adaptation, distribution and reproduction in any medium or format, as long as you give appropriate credit to the original author(s) and the source, provide a link to the Creative Commons licence, and indicate if changes were made. The images or other third party material in this article are included in the article's Creative Commons licence, unless indicated otherwise in a credit line to the material. If material is not included in the article's Creative Commons licence and your intended use is not permitted by statutory regulation or exceeds the permitted use, you will need to obtain permission directly from the copyright holder. To view a copy of this licence, visit <http://creativecommons.org/licenses/by/4.0/>.

© The Author(s) 2023